

SUPPLEMENTAL MATERIAL

Phase transitions in fluctuations and their role in two-step nucleation

D. James, S. Beairsto, C. Hartt, O. Zavalov, I. Saika-Voivod, R.K. Bowles and P.H. Poole

December 17, 2018

S1. PHASE DIAGRAM

To evaluate the phase diagram of our lattice model, we use umbrella sampling MC simulations to compute the system free energy as a function of two bulk order parameters, the magnetization m and the staggered magnetization m_s [43, 51]. These are defined as,

$$m = \frac{1}{N} \sum_{i=1}^N s_i \quad (\text{S1})$$

$$m_s = \frac{1}{N} \sum_{i=1}^N \sigma_i s_i. \quad (\text{S2})$$

Note that m and m_s are subject to the constraints,

$$\begin{aligned} m + m_s &\leq 1 \\ m - m_s &\leq 1. \end{aligned} \quad (\text{S3})$$

The order parameters m and m_s can be used to identify each of the phases in our system. At $T = 0$, four phases are observed, depending on the values of H and H_s : two ferromagnetically ordered phases with $(m, m_s) = (-1, 0)$ and $(m, m_s) = (1, 0)$, denoted respectively as $\bar{\mathcal{B}}$ and \mathcal{B} ; and two antiferromagnetically ordered phases with $(m, m_s) = (0, -1)$ and $(m, m_s) = (0, 1)$, denoted respectively as \mathcal{A} and \mathcal{C} . Since we only consider $H > 0$, the $\bar{\mathcal{B}}$ phase does not appear in our analysis.

To locate stability fields and phase boundaries for each phase, we evaluate,

$$\beta G(m_s, m) = -\log[P(m_s, m)] + C, \quad (\text{S4})$$

where $G(m_s, m)$ is the conditional free energy of the system at fixed (H_s, H, T) as a function of m_s and m . $P(m_s, m)$ is a function that is proportional to the probability of observing a

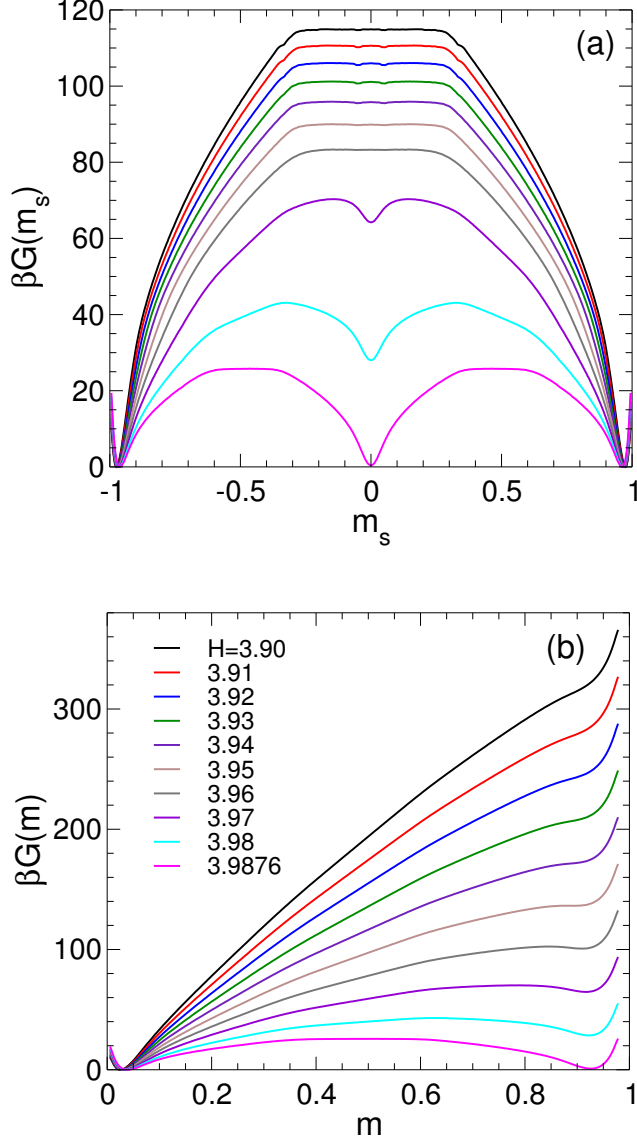


FIG. S1. (a) $G(m_s)$ and (b) $G(m)$ along the \mathcal{AC} coexistence curve (where $H_s = 0$) for a system with $L = 64$. The legend given in (b) applies to both panels.

given value of m_s and m under the same conditions of (H_s, H, T) . The value of the arbitrary constant C in Eq. S4, and in all subsequent equations in which it occurs, is always chosen so that the global minimum of the corresponding free energy is zero. We also define,

$$\begin{aligned} \beta G(m_s) &= -\log[P(m_s)] + C \\ P(m_s) &= \int_0^1 P(m_s, m) dm, \end{aligned} \quad (\text{S5})$$

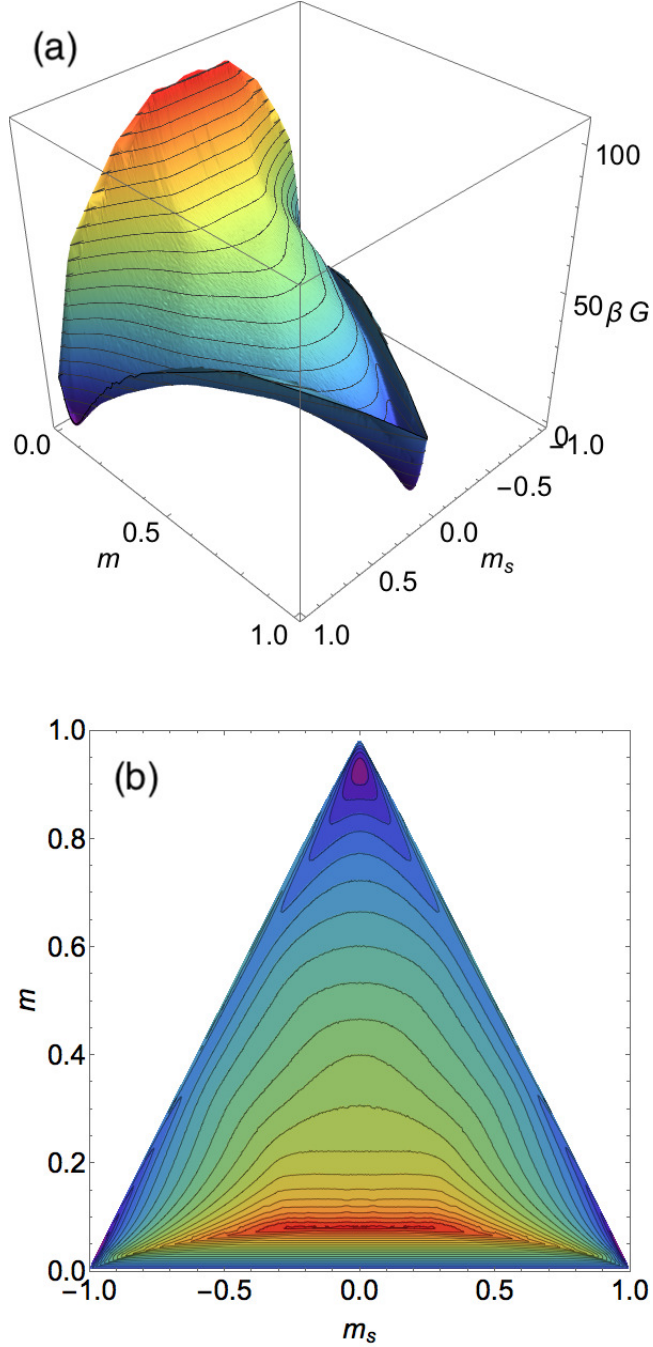


FIG. S2. $G(m_s, m)$ at the triple point for a system with $L = 64$. Contours are $5kT$ apart. Panel (a) is a surface plot of $G(m_s, m)$ and panel (b) is a contour plot of the same data.

and,

$$\begin{aligned}
 \beta G(m) &= -\log[P(m)] + C \\
 P(m) &= \int_{-1}^1 P(m_s, m) dm_s.
 \end{aligned}
 \tag{S6}$$

We estimate $P(m_s, m)$ from umbrella sampling simulations using a biasing potential,

$$U'_B = \kappa_s(m_s - m_s^*)^2 + \kappa_m(m - m^*)^2, \quad (\text{S7})$$

where m_s^* and m^* specify the target values of m_s and m to be sampled, and κ_s and κ_m control the range of sampling around the target values. All our umbrella sampling simulations using U'_B are carried out with a system size of $L = 64$ and at the state point $(H_s^0, H^0, kT/J) = (0, 3.9875, 1)$. As we will see below, this point is on the \mathcal{AC} coexistence line and is very close to the \mathcal{ABC} triple point. Since this point is on the $H_s = 0$ axis, we only need to compute $P(m_s, m)$ for $0 < m_s < 1$ because $P(m_s, m) = P(-m_s, m)$ under these conditions. Also, since $m_s + m \leq 1$, the range of $P(m_s, m)$ is further restricted to the triangle-shaped region bounded by $m_s = 0$, $m = 0$, and $m_s + m = 1$. We cover this region using 903 umbrella windows with $m_s^* = 100i/L^2$ where i is an integer in the range $[0, 41]$, and $m^* = 100j/L^2$ where j is an integer in the range $[0, 41 - i]$. We choose $\kappa_s = \kappa_m = 0.0005L^4J$. Trial configurations are accepted or rejected using the umbrella potential every 1 MCS. In all of our simulations, one MCS corresponds to L^2 attempts to flip the spin of a randomly chosen lattice site. The simulation for each umbrella window is initialized using a perfect \mathcal{C} configuration. Each run is equilibrated for 2×10^5 MCS, after which m_s and m are recorded every 400 MCS for the next 4×10^6 MCS.

The time series of m_s and m for all umbrella simulations are analyzed and combined using WHAM [55, 56] to generate estimates of $P(m_s, m)$ and $G(m_s, m)$ at $(H_s^0, H^0, kT/J) = (0, 3.9875, 1)$. For the WHAM analysis, we exclude every run with an umbrella sampling acceptance rate of less than 0.04. This reduces the number of windows analyzed to 819. The windows excluded are: $j = 0$ and $0 \leq i \leq 33$; $j = 1$ and $0 \leq i \leq 28$; and $j = 2$ and $0 \leq i \leq 20$. These windows correspond to regions in which $G(m_s, m)$ is very large and steep, and which make a negligible contribution to the average properties of equilibrium states near the triple point. We estimate that the error in our computed values for $G(m_s, m)$ is at most $1kT$.

$P(m_s, m)$ provides the complete density of states as a function of m_s and m , and can be used to find $P(m_s, m)$ or $G(m_s, m)$ at nearby values of (H_s, H) by reweighting according to,

$$G(m_s, m; H_s, H)/J = G(m_s, m; H_s^0, H^0)/J - N(H_s - H_s^0)m_s - N(H - H^0)m. \quad (\text{S8})$$

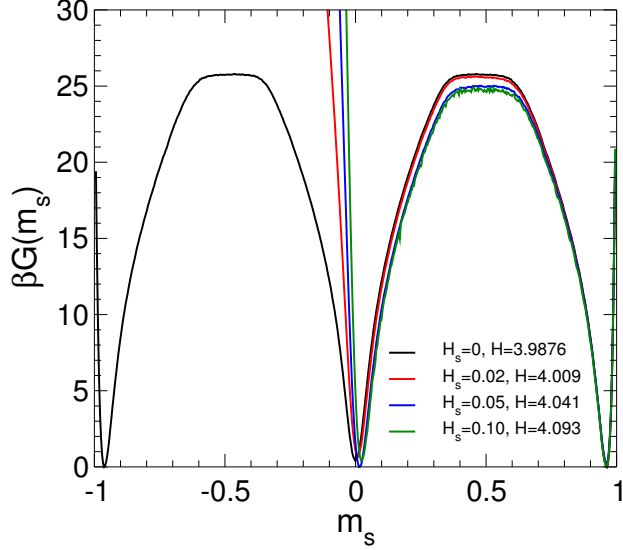


FIG. S3. $G(m_s)$ along the \mathcal{BC} coexistence curve for an $L = 64$ system.

Having reweighted $G(m_s, m)$ to new values of (H_s, H) , we can also obtain $G(m_s)$ and $G(m)$ at the same (H_s, H) .

Due to the symmetry of the system Hamiltonian, the \mathcal{AC} coexistence line lies on the $H_s = 0$ axis and so the value of H_s at the \mathcal{ABC} triple point is $H_s^T = 0$. At the triple point, $G(m_s, m)$ will exhibit three basins of approximately equal depth, one for each of the phases \mathcal{A} , \mathcal{B} and \mathcal{C} . We further note that when $H > 0$ and the $\bar{\mathcal{B}}$ phase can be ignored, m_s by itself serves as an order parameter to distinguish each phase, since $m_s \simeq -1$ in \mathcal{A} , $m_s \simeq 0$ in \mathcal{B} , and $m_s \simeq 1$ in \mathcal{C} . At the triple point, $G(m_s)$ will therefore also display three minima of approximately equal depth. In Fig. S1(a) we show $G(m_s)$ at $H_s = 0$ for several H approaching the triple point, where we observe the emergence of these three minima. To precisely locate H^T , the value of H at the triple point, we evaluate $P(m_s)$ at several values of H and seek conditions where the areas under the three peaks in $P(m_s)$ corresponding to each phase are equal [49, 50]. We find $H^T = 3.9876 \pm 0.0005$. Fig. S1 shows $G(m_s)$ and $G(m)$ at the triple point, and Fig. S2 shows $G(m_s, m)$ at the triple point.

We locate points on the \mathcal{BC} coexistence curve by examining the behavior of $G(m_s)$ and $P(m_s)$ at several fixed values of $H_s > 0$. For a given value of H_s , we seek the value of H at which the areas under the peaks in $P(m_s)$ for the \mathcal{B} and \mathcal{C} phases are equal. Fig. S3 shows $G(m_s)$ at several points on the \mathcal{BC} coexistence curve determined in this way, confirming that under these conditions the minima for the \mathcal{B} and \mathcal{C} phases are of approximately equal depth. The result for the \mathcal{BC} coexistence curve is shown in Fig. 2, for which the statistical

error in H is 0.0005. The \mathcal{AB} coexistence curve in Fig. 2 is simply the reflection of the \mathcal{BC} coexistence curve about the $H_s = 0$ axis.

S2. LIMIT OF METASTABILITY OF THE \mathcal{B} PHASE

As shown in Fig. S1(b), at $H_s = 0$ a local minimum corresponding to the \mathcal{B} phase occurs in $G(m)$ in the vicinity of $m \simeq 0.95$. This minimum persists even for values of H outside of the stability field of \mathcal{B} , i.e. for values of H below the triple point. Under these conditions, this minimum of $G(m)$ corresponds to the metastable bulk \mathcal{B} phase. As H decreases further this minimum disappears, thus defining the limit of metastability (LOM) of the bulk \mathcal{B} phase. We locate the LOM of the \mathcal{B} phase in the phase diagram by seeking the value of H at which the local minimum for \mathcal{B} in $G(m)$ disappears with decreasing H at several fixed values of H_s . The result for a system of size $L = 64$ is shown in Fig. 2. Note the LOM is system-size dependent. As $L \rightarrow \infty$, the LOM approaches the \mathcal{BC} and \mathcal{AB} coexistence curves [53].

S3. CHEMICAL POTENTIAL OF BULK PHASES AND METASTABLE PHASE BOUNDARIES

We estimate the chemical potential of each bulk phase at a given value of (H_s, H) , relative to its value at the triple point, using,

$$\bar{\mu}_{\mathcal{A}}(H_s, H) = -\frac{kT}{N} \log \left(\int_{-1}^{-0.9} dm_s \int_0^1 dm \exp[-\beta G(m_s, m; H_s, H)] \right) - \bar{\mu}_{\mathcal{A}}^0 \quad (\text{S9})$$

$$\bar{\mu}_{\mathcal{B}}(H_s, H) = -\frac{kT}{N} \log \left(\int_{-1}^1 dm_s \int_{0.9}^1 dm \exp[-\beta G(m_s, m; H_s, H)] \right) - \bar{\mu}_{\mathcal{B}}^0 \quad (\text{S10})$$

$$\bar{\mu}_{\mathcal{C}}(H_s, H) = -\frac{kT}{N} \log \left(\int_{0.9}^1 dm_s \int_0^1 dm \exp[-\beta G(m_s, m; H_s, H)] \right) - \bar{\mu}_{\mathcal{C}}^0, \quad (\text{S11})$$

where $\bar{\mu}_{\mathcal{A}}^0$ is chosen such that $\bar{\mu}_{\mathcal{A}}(H_s^T, H^T) = 0$, and similarly for $\bar{\mu}_{\mathcal{B}}^0$ and $\bar{\mu}_{\mathcal{C}}^0$. The integrals in the above relations sum over a region of the (m_s, m) plane which encompasses the minimum of the basin for the corresponding phase, and in which the system is a single homogeneous

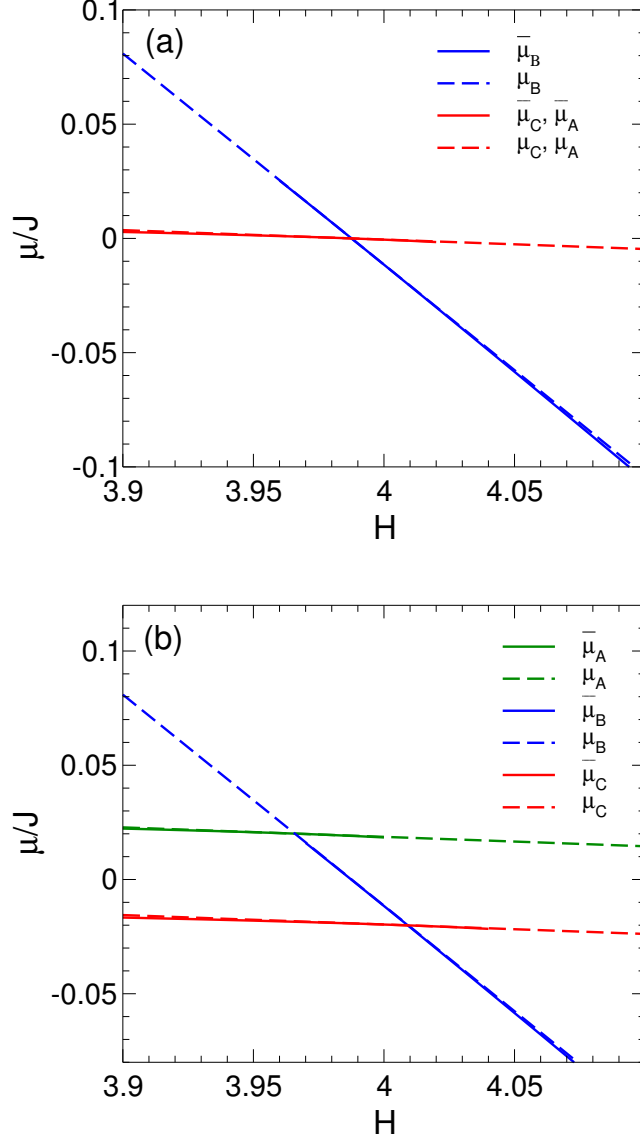


FIG. S4. Chemical potentials of bulk phases as a function of H at fixed H_s . Solid lines end at the limit of metastability for the bulk phase in a system with $L = 64$. In (a) $H_s = 0$, and in (b) $H_s = 0.02$. Note that when $H_s = 0$, $\mu_A = \mu_C$.

phase. In Fig. S4 we plot $\bar{\mu}_A$, $\bar{\mu}_B$ and $\bar{\mu}_C$ as a function of H at $H_s = 0$ and $H_s = 0.02$. These lines terminate at the value of H for the LOM of each phase for our $L = 64$ system, i.e. where the local minimum in $G(m_s, m; H_s, H)$ ceases to exist.

Although the chemical potential is always well defined within the stability field of each phase, for a metastable bulk phase it is only defined when a local minimum is observed in $G(m_s, m; H_s, H)$. However, for the purpose of analyzing the nucleation behavior predicted by Eq. 1, it would be useful to have an approximate way to assign a value to the chemical potential for a phase that is beyond its LOM. We find that it is possible to do so in our

lattice model because the dependence of $\bar{\mu}$ on H_s and H is very close to linear for all three phases; see Fig. S4. As a simple approximation, we therefore model the chemical potential for each phase, relative to the triple point, using the expressions:

$$\mu_{\mathcal{A}}(H_s, H)/J = -(H_s - H_s^T)m_s^{\mathcal{A}} - (H - H^T)m^{\mathcal{A}} \quad (\text{S12})$$

$$\mu_{\mathcal{B}}(H_s, H)/J = -(H_s - H_s^T)m_s^{\mathcal{B}} - (H - H^T)m^{\mathcal{B}} \quad (\text{S13})$$

$$\mu_{\mathcal{C}}(H_s, H)/J = -(H_s - H_s^T)m_s^{\mathcal{C}} - (H - H^T)m^{\mathcal{C}}. \quad (\text{S14})$$

In these relations, we use the value of m_s and m for each phase at the triple point to fix the rate of change of μ with H_s or H , since $m_s = -(\partial\mu/\partial H_s)_{H,T}$ and $m = -(\partial\mu/\partial H)_{H_s,T}$. At the triple point, the average value of m_s and m for the \mathcal{A} phase is $m_s^{\mathcal{A}} = -0.959$ and $m^{\mathcal{A}} = 0.0413$; for the \mathcal{B} phase is $m_s^{\mathcal{B}} = 0$ and $m^{\mathcal{B}} = 0.924$; and for the \mathcal{C} phase is $m_s^{\mathcal{C}} = -m_s^{\mathcal{A}}$ and $m^{\mathcal{C}} = m^{\mathcal{A}}$. We compare $\bar{\mu}$ and μ for each phase in Fig. S4, and find that these two approaches give nearly indistinguishable results. The metastable extensions of the coexistence boundaries shown in Fig. 2 are estimated by finding the intersection of the surfaces defined in Eqs. S12-S14.

Note that since $m^{\mathcal{C}} = m^{\mathcal{A}}$, then $\Delta\mu_{\mathcal{AC}} = \mu_{\mathcal{C}} - \mu_{\mathcal{A}}$ does not depend on H and is constant at fixed H_s . In contrast, $\Delta\mu_{\mathcal{AB}} = \mu_{\mathcal{B}} - \mu_{\mathcal{A}}$ decreases linearly with H at fixed H_s . These observations are relevant for understanding the behavior of the CNT estimates for $n_{\mathcal{AB}}^*$ and $n_{\mathcal{AC}}^*$ plotted in Fig. 11.

S4. SURFACE TENSION

The surface tension (or interfacial free energy) σ between two coexisting phases can be estimated from the height of the free energy barrier that separates the two successive minima corresponding to the coexisting phases in a plot of $G(m_s)$ or $G(m)$ [50, 52, 53]. This approach provides a direct estimate of the surface tension because the free energy is evaluated as a function of an order parameter which is a continuous reaction coordinate connecting a free energy minimum, where the system is a single homogeneous phase, to a free energy maximum, where the systems consists of two coexisting phases separated by an interface. The thermodynamic work of formation of the interface is thus computed directly. As shown in Figs. S1 and S3, the top of this free energy barrier is flat for a system in

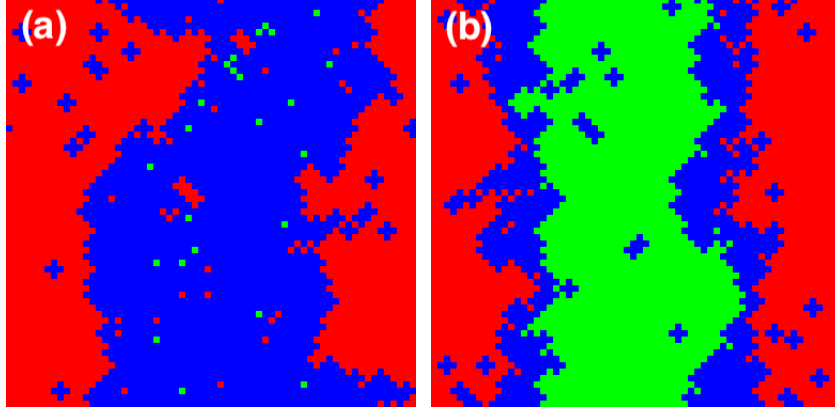


FIG. S5. (a) Snapshot of \mathcal{BC} coexistence at $H_s = 0$ and $H = 3.987$ in a system with $m_s \simeq 0.5$. (b) Snapshot of \mathcal{AC} coexistence at $H_s = 0$ and $H = 3.96$ in a system with $m_s \simeq 0$. $L = 64$ for both (a) and (b).

which two phases coexist, indicating the range of m_s or m values where two flat interfaces separate the two phases in our periodic system. Example snapshots of coexisting phases in our $L = 64$ simulations are shown in Fig. S5.

We define the interfacial free energy σ such that the height of the barrier in $\beta G(m_s)$ or $\beta G(m)$ is $2L\beta\sigma$; the factor of $2L$ accounts for the two interfaces that occur in a system with periodic boundaries. Fig. S3 shows that for the coexistence of \mathcal{B} and \mathcal{C} in a $L = 64$ system at the triple point conditions, $2L\beta\sigma_{\mathcal{BC}} = 25 \pm 1$, and exhibits little observable variation along the \mathcal{BC} coexistence curve in the range of H and H_s studied here.

In Fig. S6 we show $G(m)$ for various H at $H_s = 0$. For any H , $\sigma_{\mathcal{BC}}$ may be estimated from the difference between the $G(m)$ curve and a common-tangent line bounding the $G(m)$ curve from below, at a value of m corresponding to a coexisting system of \mathcal{B} and \mathcal{C} , e.g. $m = 0.5$. Further, at fixed H_s , if $G(m)$ is computed at one value of $H = H_1$, it can be found (up to an irrelevant constant C) at a new value $H = H_2$ using,

$$G(m; H_2)/J = G(m; H_1)/J - N(H_2 - H_1)m + C. \quad (\text{S15})$$

As a consequence of the form of Eq. S15, $\sigma_{\mathcal{BC}}$ is independent of H at fixed H_s . Also, since we have observed that $\sigma_{\mathcal{BC}}$ varies little on the \mathcal{BC} coexistence curve (Fig. S3), along which H_s is changing, we conclude that $\sigma_{\mathcal{BC}}$ is approximately constant for all H and H_s studied here.

Note that we obtain the same value of $\sigma_{\mathcal{BC}}$ (within error) when we analyze the height

of the barrier observed in either $G(m_s)$ in Fig. S3, or $G(m)$ in Fig. S6. This confirms that our estimate of the surface tension does not depend on the choice of m or m_s as the order parameter to distinguish between the \mathcal{B} phase and either of the \mathcal{A} or \mathcal{C} phases.

Furthermore, the symmetry of the system Hamiltonian ensures that $\sigma_{\mathcal{AB}} = \sigma_{\mathcal{BC}}$. That is, the \mathcal{A} and \mathcal{C} phases are structurally identical in that both are antiferromagnetic “checkerboard” phases. The only difference is that in the \mathcal{C} phase the spins are aligned with a positive staggered field, while in the \mathcal{A} phase they are anti-aligned. Thus the average structure of the interface of either the \mathcal{A} or \mathcal{C} phase with the all-up \mathcal{B} phase is the same; in either case, the interface is the boundary between a checkerboard phase and an all-up phase. The equality $\sigma_{\mathcal{AB}} = \sigma_{\mathcal{BC}}$ is numerically confirmed at the triple point in Fig. S1(a), where we see that the heights of the two free energy maxima in $G(m_s)$, which directly measure $\sigma_{\mathcal{AB}}$ and $\sigma_{\mathcal{BC}}$, are equal. Since we have also shown that $\sigma_{\mathcal{BC}}$ is independent of H and H_s , we can conclude that $\sigma_{\mathcal{AB}} = \sigma_{\mathcal{BC}}$ throughout our phase diagram. We thus use the value $2L\beta\sigma_{\mathcal{AB}} = 2L\beta\sigma_{\mathcal{BC}} = 25$, or $\sigma_{\mathcal{AB}}/J = \sigma_{\mathcal{BC}}/J = 0.195$ (per unit lattice site of interface) in all of our analysis.

We next estimate $\sigma_{\mathcal{AC}}$ as a function of H along the $H_s = 0$ axis for $H < H_T$. In Fig. S1(a) we plot $G(m_s)$ on the \mathcal{AC} coexistence curve at $H = 3.94$, a point at which the \mathcal{B} phase is unstable for a system of size $L = 64$. From the height of the free energy barrier separating the minima corresponding to the pure \mathcal{A} and \mathcal{C} phases, we find $2L\beta\sigma_{\mathcal{AC}} = 96 \pm 1$. We also directly estimate $\sigma_{\mathcal{AC}}$ for other values of H from the $G(m_s)$ curves in Fig. S1 that are flat near $m_s = 0$, and plot the results in Fig. S7.

To estimate $\sigma_{\mathcal{AC}}$ as a function of H along the entire \mathcal{AC} coexistence curve we use thermodynamic integration. That is, we choose as a reference value $H_0 = 3.94$ where we already know $\sigma_{\mathcal{AC}}$ from the direct calculation described above. We then use thermodynamic integration to estimate the change in the interfacial free energy as we move the system to a different value of H . On the \mathcal{AC} coexistence curve, the free energy of the pure \mathcal{A} and \mathcal{C} phases is the same. Under these conditions, the \mathcal{AC} surface tension is the difference between the free energy of a system containing an \mathcal{AC} interface and the free energy of a pure phase, either \mathcal{A} or \mathcal{C} , since the conversion of part of the system from \mathcal{A} to \mathcal{C} to create the coexisting system makes no bulk contribution to the free energy change. The change in the \mathcal{AC} surface tension on moving from H_0 to H is thus given by the difference between the change in the free energy of a system containing an \mathcal{AC} interface, and the change in the free energy of the

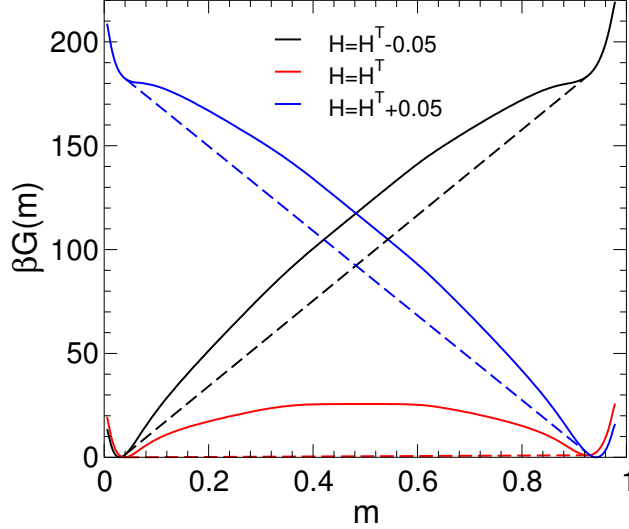


FIG. S6. $G(m)$ at $H_s = 0$ at various H for system size $L = 64$. Dashed lines are common tangent constructions for each $G(m)$ curve.

pure phase:

$$2L\sigma_{\mathcal{AC}}(H) - 2L\sigma_{\mathcal{AC}}(H_0) = \Delta G_{\text{coex}}(H) - \Delta G_{\mathcal{A}}(H). \quad (\text{S16})$$

The change in the free energy of a system containing an \mathcal{AC} interface on moving from H_0 to H is given by,

$$\Delta G_{\text{coex}}(H)/J = -N \int_{H_0}^H m_{\text{coex}}(H') dH'. \quad (\text{S17})$$

Here $m_{\text{coex}}(H)$ is the average magnetization of a system containing an \mathcal{AC} interface as a function of H . To estimate $m_{\text{coex}}(H)$, we evaluate m as a function of H for a coexisting system of \mathcal{A} and \mathcal{C} phases along the $H_s = 0$ coexistence curve. We constrain this coexisting system to remain within the range of m_s consistent with the occurrence of a pair of system-spanning \mathcal{AC} interfaces by applying a simple square-well biasing potential that prevents the system from sampling microstates with $|m_s| > 0.1$. In Eq. S16 we chose \mathcal{A} to represent the pure phase. Its free energy change on moving from H_0 to H is given by,

$$\Delta G_{\mathcal{A}}(H)/J = -N \int_{H_0}^H m_{\mathcal{A}}(H') dH', \quad (\text{S18})$$

where $m_{\mathcal{A}}(H)$ is the average magnetization of the pure \mathcal{A} phase as a function of H . To estimate $m_{\mathcal{A}}(H)$, we evaluate m as a function of H for the homogeneous \mathcal{A} phase along the $H_s = 0$ coexistence curve.

The result for $\sigma_{\mathcal{AC}}$ is shown in Fig. S7. We show snapshots of the coexisting \mathcal{A} and \mathcal{C}

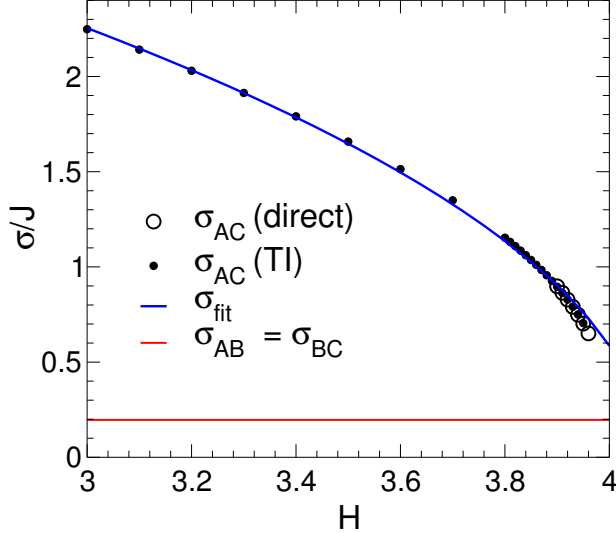


FIG. S7. Interfacial tensions versus H at $H_s = 0$ for $L = 64$. Open circles are values of $\sigma_{\mathcal{AC}}$ found directly from the plots of $G(m_s)$ presented in Fig. S1(a). Filled circles are values of $\sigma_{\mathcal{AC}}$ found by thermodynamic integration (TI) using Eq. S16. The blue curve is $\sigma_{\text{fit}}/J = (19.299 - 4.739H)^{1/2}$, fitted to data obtained via TI for $H = 2$ to $H = 4$. The red curve gives the value of $\sigma_{\mathcal{AB}} = \sigma_{\mathcal{BC}}$.

phases at different values of H in Fig. S8. We note the complexity of the \mathcal{AC} interface. Depending on H the interface may contain a significant wetting layer of \mathcal{B} between the \mathcal{A} and \mathcal{C} regions. Approaching the triple point $\sigma_{\mathcal{AC}}$ decreases but remains more than twice the value of $\sigma_{\mathcal{AB}}$ at the triple point. Given the emergence of the wetting layer of \mathcal{B} as $H \rightarrow H^T$, the behavior of $\sigma_{\mathcal{AC}}$ makes sense: In this regime the \mathcal{AC} interface can be approximated as the superposition two interfaces, one \mathcal{AB} and the other \mathcal{BC} . Since $\sigma_{\mathcal{AB}} = \sigma_{\mathcal{BC}}$, it therefore seems likely that the condition $\sigma_{\mathcal{AC}} \geq 2\sigma_{\mathcal{AB}}$ holds under all conditions studied here.

In order to compare the behavior of our lattice model to the predictions of CNT, it is useful to have an analytic model of the dependence of $\sigma_{\mathcal{AC}}$ on H_s and H throughout the phase diagram. By an argument analogous to that used above to establish that $\sigma_{\mathcal{BC}}$ is independent of H at constant H_s (see Eq. S15), it can be shown that $\sigma_{\mathcal{AC}}$ is independent of H_s at fixed H . To model the dependence of $\sigma_{\mathcal{AC}}$ on H , we notice empirically that $\sigma_{\mathcal{AC}}^2$ is approximately linear in H between $H = 2$ and 4. We fit a straight line to our data for $\sigma_{\mathcal{AC}}^2$ in this range and obtain $\sigma_{\text{fit}}/J = (19.299 - 4.739H)^{1/2}$, shown in Fig. S7. We use σ_{fit} to compute the CNT estimate of $n_{\mathcal{AC}}^*$ plotted in Fig. 11.

We note that our quantitative estimates for σ should be considered preliminary. All of our estimates for σ are based on square systems with $L = 64$, and assume an interface that is, on average, flat and oriented parallel to a lattice axis. A more detailed and accurate

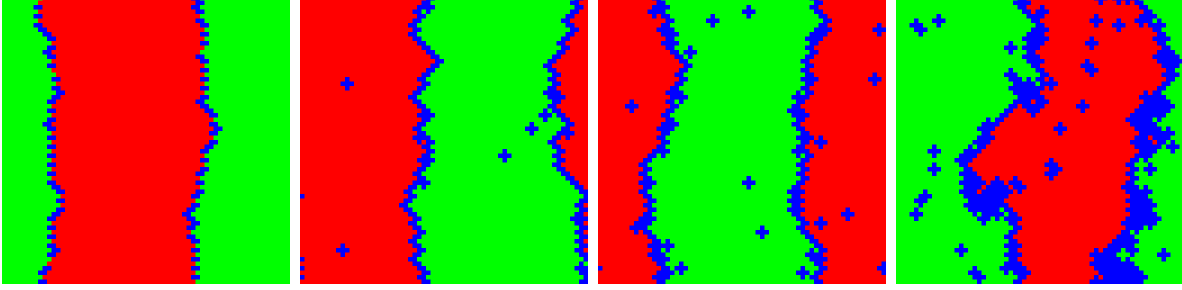


FIG. S8. Snapshots of \mathcal{AC} coexistence when $L = 64$ and $H_s = 0$ for various $H = \{1.0, 3.0, 3.5, 3.9\}$, from left to right.

analysis is possible by monitoring system-size effects, the influence of the system shape and boundary conditions, as well as considering the influence of the orientation of the interface to the lattice axes [52]. That said, for the purposes of this work, it is sufficient that we have shown that $\sigma_{AB} < \sigma_{AC}$ throughout the range of the phase diagram studied here.

Fig. S9 compares our direct numerical evaluation of $\bar{G}(n)$ at state point (f) in Table I with the CNT predictions for G_{AB} and G_{AC} as defined in Eq. 1 and calculated using the corresponding values of μ and σ given in Table I. These values of μ and σ are estimated for each phase or interface as described above. The shape of the curve for $\bar{G}(n)$ is similar to G_{AB} for $n < n_c$, and to G_{AC} for $n > n_c$, confirming the qualitative predictions of the CNT analysis in Section II. However, significant quantitative differences occur at all values of n . These differences likely arise from several sources. For example, the CNT expression in Eq. 1 for the nucleation barrier is known to deviate significantly from the numerically computed barrier even for simple lattice models such as ours [54]. Also, as noted above, we have used values of the surface tension as estimated for flat interfaces that are aligned with a lattice axis. At small n , where the interface is strongly curved, we expect this approximation to introduce significant deviations, which will manifest at larger n as an offset between the predicted and the observed curves.

S5. IDENTIFYING LOCAL FLUCTUATIONS OCCURRING WITHIN THE \mathcal{A} PHASE

Here we focus on the \mathcal{A} phase, and develop a definition for identifying local regions that deviate in structure from that expected in the \mathcal{A} phase.

In the perfect \mathcal{A} phase, all sites satisfy $s_i = -\sigma_i$. In the perfect \mathcal{C} phase, all sites satisfy

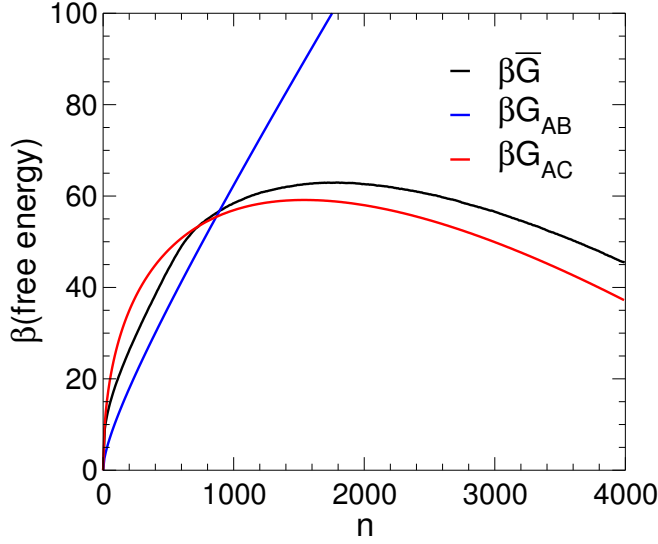


FIG. S9. Comparison of: $\bar{G}(n)$ for $L = 128$, $H=3.92$, and $H_s = 0.02$; and G_{AB} and G_{AC} as computed using Eq. 1 using the values of the chemical potentials and surface tensions as found in Table I for state point (f).

$s_i = \sigma_i$. In the perfect \mathcal{B} phase, all sites satisfy $s_i = 1$. We therefore define a local fluctuation occurring within the \mathcal{A} phase as any contiguous cluster of sites for which $s_i = \sigma_i$ or $s_i = 1$. The one exception to this definition is a single site at which $s_i = 1$ and for which all 4 nn's have $s_i = -1$. Half of the sites in the perfect \mathcal{A} phase have this property, and we exclude them from our definition of a fluctuation. An example system configuration is shown in Fig. S10, and illustrates our cluster definition.

The number of sites in a cluster is denoted by n . The number of sites in the largest cluster in the system is n_{\max} . The composition of a cluster is defined as $f = \bar{n}/n$, where \bar{n} is the number of sites in the cluster that correspond to the \mathcal{C} phase. We define $\bar{n} = 2n_{\text{down}}$, where n_{down} is the number of cluster sites for which $s_i = -1$. The reason for this definition of f is that cluster sites satisfying $s_i = 1$ may also satisfy $s_i = \sigma_i$, and so it is ambiguous if these sites belong to the fraction of sites inside the cluster that belong to the \mathcal{C} phase or to the \mathcal{B} phase. Since cluster sites with $s_i = -1$ unambiguously belong to the \mathcal{C} phase, and since the fraction of $s_i = -1$ sites in the perfect \mathcal{C} phase is $1/2$, we estimate the total number of \mathcal{C} sites within a cluster to be $2n_{\text{down}}$. The quantity f therefore characterizes the cluster composition in terms of how much of the cluster is taken up by the \mathcal{C} phase: $f = 0$

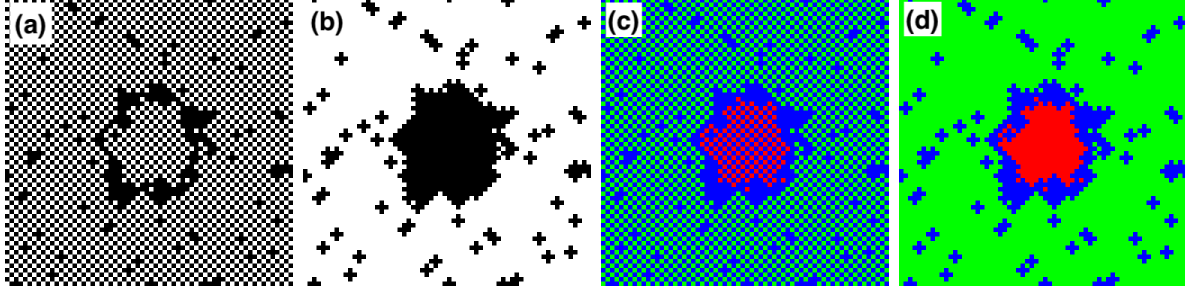


FIG. S10. Example $L = 64$ system configuration. (a) White sites satisfy $s_i = -1$. Black sites satisfy $s_i = 1$. (b) Black sites satisfy the definition for belonging to a fluctuation. White sites do not. (c) Green sites satisfy $s_i = -1 = -\sigma_i$. Blue sites satisfy $s_i = 1$. Red sites satisfy $s_i = -1 = \sigma_i$. (d) Same as (c), except that all blue sites in (c) totally surrounded by green sites are rendered as green in (d); and all blue sites in (c) totally surrounded by red sites are rendered as red in (d).

is a pure \mathcal{B} cluster, while $f = 1$ is a pure \mathcal{C} cluster.

We note that cluster sites with $s_i = 1$ on the cluster perimeter are always considered part of the cluster, even though half of them (on average) might reasonably be associated with the surrounding \mathcal{A} phase. For computational efficiency, we do not apply this correction, which if implemented would decrease the values of n and n_{\max} from those used here.

For visualization purposes, we render system configurations as shown in Fig. S10(d). The rules we use to assign a color to each site are stated in the figure caption. In the resulting color scheme, the \mathcal{A} phase is green, the \mathcal{B} phase is blue, and the \mathcal{C} phase is red.

S6. 2D UMBRELLA SAMPLING SIMULATIONS TO FIND $G(n_{\max}, f)$

$G(n_{\max}, f)$ is estimated from 2D umbrella sampling simulations using the biasing potential given in Eq. 6. We choose $\kappa_n = 0.0005$ and $\kappa_f = 500$. For each choice of (L, H_s, H, T) we conduct 900 simulations for $n_{\max}^* = 100i$ where the integer $i \in [0, 99]$, and for $f^* = j/10$ where the integer $j \in [0, 8]$. Each run is initiated from a perfect \mathcal{A} configuration, into which a seed cluster is inserted. The seed cluster is a square of sites with $s_i = 1$ of a size chosen to be closest to n_{\max}^* . At the centre of the seed cluster there is a square region with $s_i = \sigma_i$ of a size chosen so that the seed cluster has a value of f closest to f^* . This system is equilibrated for 5×10^4 MCS, and then the time series of n_{\max} and f is recorded every 100 MCS for 10^6 MCS. Trial configurations are accepted or rejected using the umbrella potential every 1 MCS. One MCS corresponds to L^2 attempts to flip the spin of a randomly chosen lattice site. Our time series for n_{\max} and f are analyzed using WHAM to evaluate $P(n_{\max}, f)$ and

$G(n_{\max}, f)$. We estimate that the error in $G(n_{\max}, f)$ is not more than $1kT$. We exclude from the WHAM analysis any run for which the acceptance rate for the umbrella sampling is less than 0.1, which occurs in a few cases when the local variation of $G(n_{\max}, f)$ is very steep. Our system size for these 2D umbrella sampling runs is $L = 128$ or 200 , as indicated in the legends or captions of the figures.

S7. 1D UMBRELLA SAMPLING SIMULATIONS TO FIND $G(n_{\max})$

To estimate n_c and n^* over a wide range of H_s and H , we conduct 1D umbrella sampling simulations in which n_{\max} alone is constrained. In this approach, we directly compute $G_1(n_{\max})$ using,

$$\beta G_1(n_{\max}) = -\log[P_1(n_{\max})] + C, \quad (\text{S19})$$

where $P_1(n_{\max})$ is proportional to the probability to observe a microstate with a given value of n_{\max} . We find n^* from the maximum in $G_1(n_{\max})$. We also monitor f during these runs, which allows us to compute χ and thus to find n_c from the maximum in χ .

To proceed, we use a biasing potential,

$$U_B'' = \kappa_n (n_{\max} - n_{\max}^*)^2, \quad (\text{S20})$$

where $\kappa_n = 0.002$. Trial configurations are accepted or rejected using the umbrella potential every 1 MCS. Each run is initiated from a perfect \mathcal{A} configuration, into which a seed cluster is inserted. The seed cluster is a square of sites with $s_i = 1$ of a size chosen to be closest to n_{\max}^* . We carry out runs using $L = 64$ or 128 , as indicated in the legends or captions of the figures. For each choice of (L, H_s, H, T) , we conduct simulations for each value of $n_{\max}^* = 50i$ where the integer $i \in [0, 24]$ when $L = 64$, and $i \in [0, 80]$ when $L = 128$. Each simulation is equilibrated for 5×10^4 MCS, and then the time series of n_{\max} is recorded every 100 MCS for 10^6 MCS. These time series are analyzed using WHAM to evaluate $P_1(n_{\max})$ and $G_1(n_{\max})$. We exclude from the WHAM analysis any runs for which the acceptance rate for the umbrella sampling is less than 0.1. As shown in Fig. 12, we use these 1D umbrella sampling runs to evaluate n_c and n^* for H_s in the range $[0.01, 0.10]$ and H in the range $[3.7, 4.0]$.

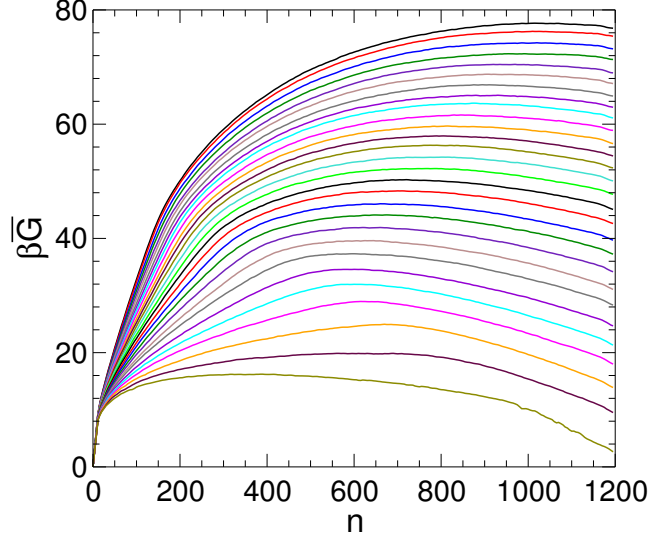


FIG. S11. $\bar{G}(n)$ for $L = 64$ and $H_s = 0.04$. $H = 3.70$ to 3.97 in steps of 0.01 , from top to bottom.

S8. HEIGHT OF THE NUCLEATION BARRIER

An example of the data used to find the locus along which $\beta G^* = 20$ is shown in Fig. S11. Here we show $\bar{G}(n)$ for several values of H at $H_s = 0.04$. We obtain G^* from the maxima of these curves, and by interpolation identify the value of H at which $\beta G^* = 20$. The locus of points in the (H_s, H) plane at which $\beta G^* = 20$ is shown in Fig. 2.

S9. FINDING n_c FROM χ

Fig. S12(a) reproduces the data for G_B and G_C from Fig. 9(a), in which the crossing of these two curves identifies n_c . Fig. S12(b) shows χ as a function of n_{\max} for the same three cases shown in Fig. S12(a). We find that the maximum of χ corresponds within error to the value of n_c obtained by finding the intersection of G_B and G_C . Based on this correspondence, all values of n_c reported in this work are computed by finding the maximum of χ . This definition allows us to estimate n_c from both 1D and 2D umbrella sampling simulations.

S10. ADDITIONAL PLOTS OF $G(n_{\max}, f)$

We present in Figs. S13 and S14 surface and contour plots of $G(n_{\max}, f)$ over additional values of H between 3.960 and 3.985 .

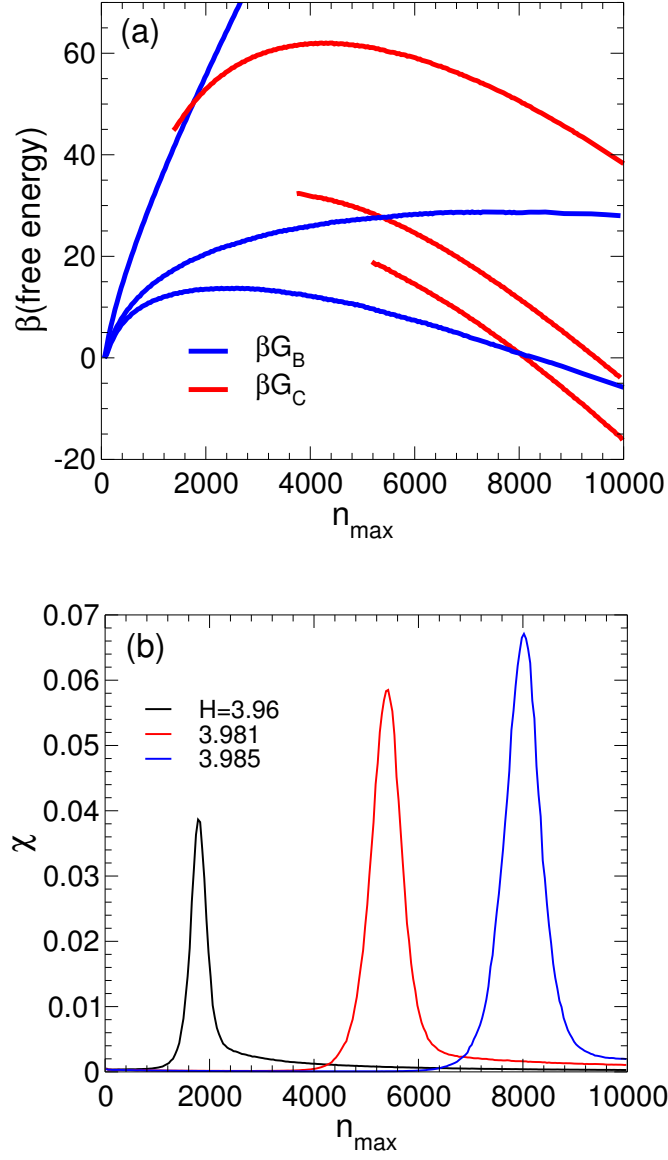


FIG. S12. (a) G_B and G_C for $H_s = 0.01$ and $L = 200$. From top to bottom $H = \{3.96, 3.981, 3.985\}$
 (b) χ for $H_s = 0.01$ and $L = 200$. From left to right $H = \{3.96, 3.981, 3.985\}$.

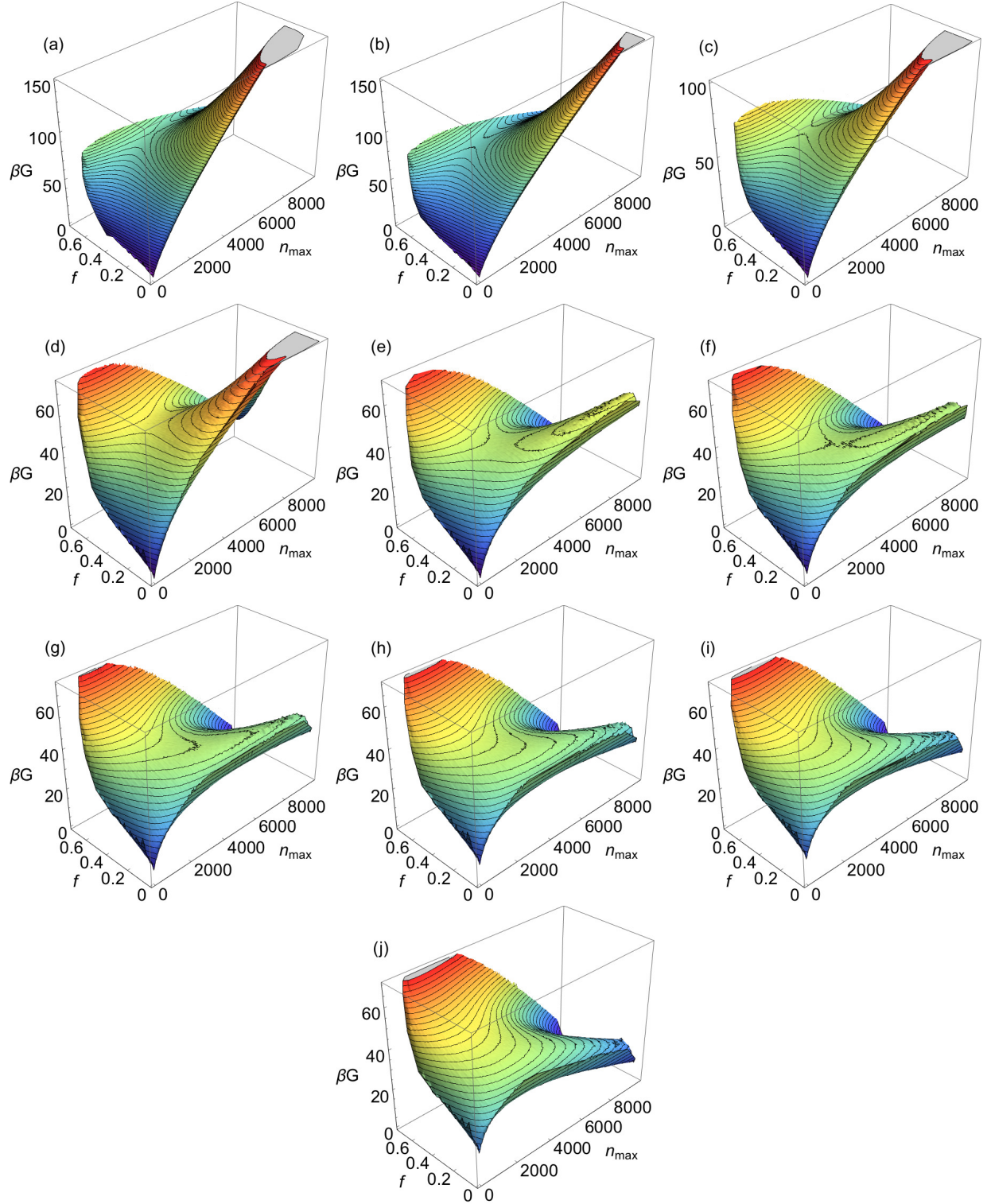


FIG. S13. $G(n_{\max}, f)$ for $H_s = 0.01$ and $L = 200$. Panels (a) through (j) correspond respectively to $H = \{3.96, 3.965, 3.97, 3.975, 3.98, 3.981, 3.982, 3.983, 3.984, 3.985\}$. Contours are $2kT$ apart.

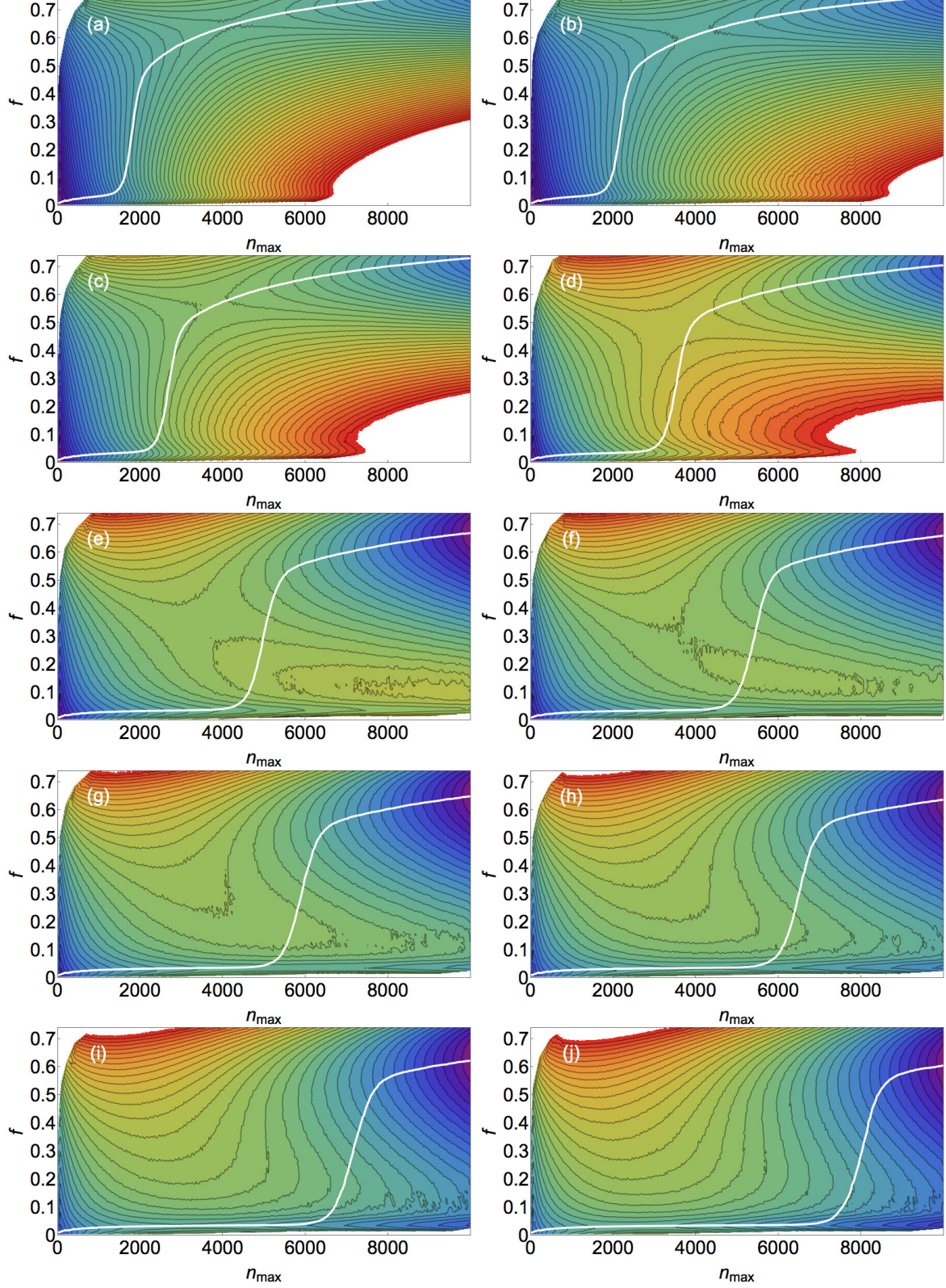


FIG. S14. $G(n_{\max}, f)$ for $H_s = 0.01$ and $L = 200$. The white line is $\langle f \rangle$. Panels (a) through (j) correspond respectively to $H = \{3.96, 3.965, 3.97, 3.975, 3.98, 3.981, 3.982, 3.983, 3.984, 3.985\}$. Contours are $2kT$ apart.